JGR Solid Earth

RESEARCH ARTICLE
10.1029/2018JB017135

Key Points:
- We present a new analysis method of GPS-acoustic observation data for seafloor positioning in the presence of sloping sound speed structure
- The application to the 2011 Tohoku earthquake demonstrate enhanced position accuracy by the spatially coherent postseismic movements
- The occurrence of episodic slow slip in 2015, which has been inferred from repeating earthquakes, was also verified from our observations

Supporting Information:
- Supporting Information S1
- Table S1
- Table S2

Correspondence to:
C. Honsho,
chie.honsho.b7@tohoku.ac.jp

Citation:
Honsho, C., Kido, M., Tomita, F., & Uchida, N. (2019). Offshore postseismic deformation of the 2011 Tohoku earthquake revisited: Application of an improved GPS-acoustic positioning method considering horizontal gradient of sound speed structure. *Journal of Geophysical Research: Solid Earth*, *124*, 5990–6009. https://doi.org/10.1029/2018JB017135

Received 17 DEC 2018
Accepted 3 MAY 2019
Accepted article online 9 MAY 2019
Published online 17 JUN 2019

Offshore Postseismic Deformation of the 2011 Tohoku Earthquake Revisited: Application of an Improved GPS-Acoustic Positioning Method Considering Horizontal Gradient of Sound Speed Structure

C. Honsho[1], M. Kido[2], F. Tomita[3], and N. Uchida[1]

[1]Research Center for Prediction of Earthquakes and Volcanic Eruptions, Graduate School of Science, Tohoku University, Sendai, Japan, [2]International Research Institute of Disaster Science, Tohoku University, Sendai, Japan, [3]Graduate School of Science, Hokkaido University, Sapporo, Japan

Abstract One of the important issues on the GPS-acoustic (GPS-A) observation for sea bottom positioning is how to address the horizontal heterogeneity of the sound speed in oceans. This study presents an analysis method of GPS-A data in the presence of a sloping sound speed structure. By applying this method and revising the analysis scheme to make full use of existing data, we reevaluated the horizontal postseismic deformations occurring ~1.5–5 years after the 2011 Tohoku earthquake. The revised horizontal movements have more uniform directions and rates between neighboring sites, suggesting enhancement of the array positioning accuracy. The revised displacement rate of the site on the incoming Pacific plate, located ~100 km northeast of the main rupture zone, was decreased significantly; it was only slightly, by 1.4 cm/year larger than the global motion of the Pacific plate, suggesting a relatively small effect of viscoelastic relaxation. The horizontal movements of the near-trench sites above the main rupture zone were generally landward and were significantly faster than the Pacific plate motion, indicating a viscoelastic relaxation of 5–10 cm/year. The distribution of the fast landward movements peaked near 38°N at an updip of the mainshock hypocenter and extended significantly farther to the north than to the south. This implies the existence of a secondary coseismic slip patch in the northern area in addition to a primary slip patch at ~38°N. The occurrence of episodic slow slip in early 2015 to the north of the main rupture zone was also verified from the GPS-A analyses.

1. Introduction

Since the GPS-acoustic (GPS-A) technique for seafloor geodesy was devised in the 1980s (Spiess, 1985), it has been developed by several research groups and has yielded many significant results for geoscience (e.g., Chadwell & Spiess, 2008; Fujita et al., 2006; Gagnon et al., 2005;Ikuta et al., 2008; Kido et al., 2006; Kido et al., 2011; Matsumoto et al., 2006; Tadokoro et al., 2006; Sato et al., 2011; Watanabe et al., 2014; Sun et al., 2014; Tomita, 2018; Tomita et al., 2015, 2017; Yokota et al., 2016; Yasuda et al., 2014, 2017). It has become necessary to enhance the accuracy of the positioning and to realize more efficient observations with an increasing number of seafloor benchmarks. One of the important issues is how to address the horizontal heterogeneity of the sound speed in oceans. In most of the aforementioned previous studies, a horizontally stratified structure was assumed for the sound speed. Although this assumption is primarily valid, some horizontal variation in the sound speed are present in actuality and can cause systematic errors in array positions of as much as several centimeters (e.g., Kido, 2007).

The effect of horizontal variation in sound speed on the array positioning is illustrated in Figure 1 through a degenerated two-dimensional (2-D) case including a two-transponder array on a flat seafloor. When observing above the array center, the travel times to the two transponders should be equal as long as the sound speed structure is horizontally stratified. However, if the sound speed actually has horizontal variation to a certain depth and is assumed to be slower toward the right side of the figure, a smaller travel time should be obtained for the left transponder than for the right one. The position of the array should appear more to the right than its actual location if a horizontally stratified structure is postulated. As the example clearly shows, an essential effect of horizontal variation is the difference in travel time delay between transponders.

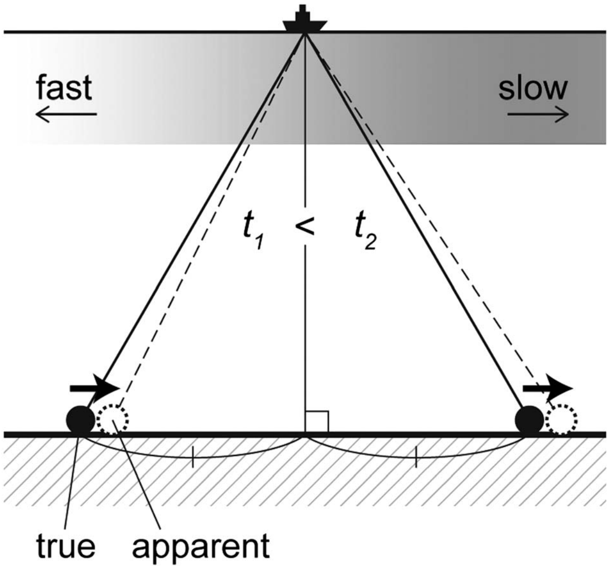

Figure 1. Schematic drawing showing the effect of horizontal variation in the sound speed on the array positioning.

Horizontal heterogeneity in the sound speed is caused by several factors such as internal waves, a sloping temperature distribution, and the presence of anomalous water masses. Internal waves were generally observed in GPS-A observations as time fluctuations in sound speed for periods of several tens of minutes to a few hours (e.g., Kido et al., 2006; Spiess et al., 1998; Tomita et al., 2015). However, phenomena at such short time scales have only an insignificant effect on the array positioning because generally, an observation time of 10 to 20 hr is devoted to a single campaign to compensate for the effects of short-period fluctuation. Of greater importance are phenomena under a steady state or at long time scales that can leave horizontal bias in the sound speed structure during the observation time.

In this study, we develop a method of array positioning that considers a persistent horizontal gradient as a first-order approximation of horizontal variation in the sound speed. We consider that the effect of variations whose wavelength is not long enough (<~10 km) to approximate them as linear variations within the scale of the array dimension would be less significant, because they are expected to be relatively short-lived, and therefore, their effect on the array position would be largely canceled out by usual observation periods of 10–20 hr. The problem setting is similar to that described in previous works by Kido (2007), Yasuda et al. (2017), and Yokota et al. (2018a), although they assumed a specific observation style or sound speed structure. It is shown herein that the effects of the gradient are finally integrated into two independent quantities despite the assumption of a more generalized sloping structure. In addition, we explain the relationship between our approach and the previous methods in the formulation of gradient effects and the application to actual data. By applying the proposed method and using an improved analysis scheme to make full use of existing data (Honsho & Kido, 2017), we reevaluate the offshore postseismic deformation following the 2011 Tohoku earthquake by revising and updating our previous results of horizontal movement (Tomita et al., 2017). Finally, we discuss the implications of our results on viscoelastic relaxation, coseismic slip, and afterslip associated with the Tohoku earthquake.

2. Observation and Data Collection

2.1. Observation Sites and Campaigns

We conducted 124 campaigns in total at 20 sites, G01–G20, located along the Japan trench at latitude 36–41°N from September 2012 to September 2016, approximately 1.5–5.5 years after the 2011 Tohoku earthquake (Figures 2a and 2b). Nine campaigns have been newly added to the former study of Tomita et al. (2017): four campaigns in each of Cruises #9 and #12 and one, at site G11, in Cruise #1. Three to six precision acoustic transponders (PXPs) were placed on the seafloor for each site, forming a square or triangle (inset of Figure 2a) with a horizontal dimension comparable to the water depth. Each site was surveyed approximately six times on average every 6 to 12 months. The present study was motivated by the necessity to enhance the accuracy of the array position in each campaign and thus to compensate for insufficient observation frequency. Our group focused more on the fixed-point surveys above the array center (Spiess, 1985; Spiess et al., 1998) than the moving surveys and thus typically spent at least 10 hr on the former and several hours on the latter during a single campaign. In certain campaigns, a moving survey was not conducted owing to limited ship time. As demonstrated subsequently, moving surveys are required in principle to apply the method considering the gradient of the sound speed. As a result, 23 of the 124 campaigns were eliminated from the analysis considering the gradient, as shown by the gray-filled circles in Figure 2b.

2.2. GPS Antenna Position, Ship Attitude, and Travel Time Data

The data set used in this study is essentially the same as that used by Tomita et al. (2017). Because the data acquisition has been described in detail by Tomita et al. (2015, 2017), only a brief outline is provided here. The GPS antenna position was determined to be 2 Hz as measured through long-baseline kinematic GPS analysis using interferometric translocation software (Colombo, 1998). The International Terrestrial

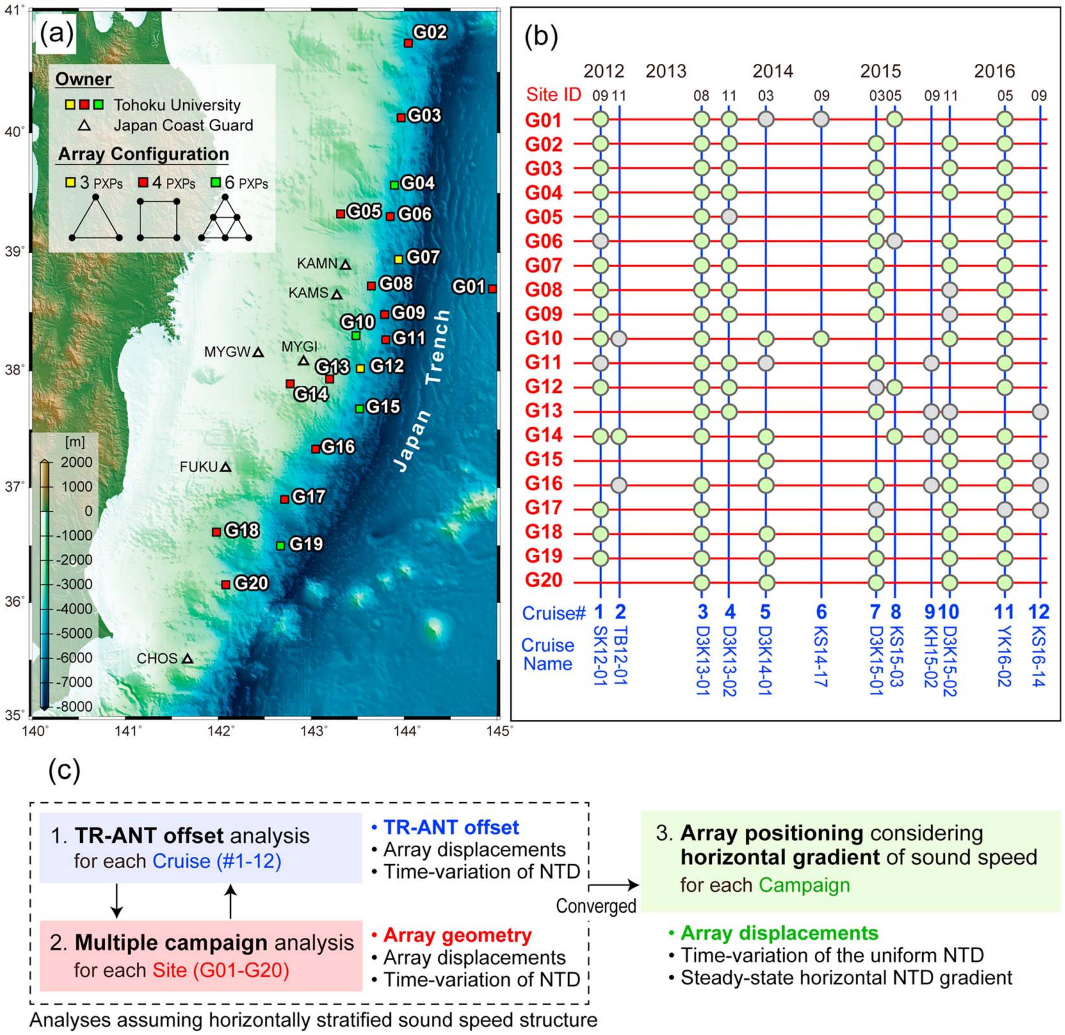

Figure 2. Overview of this study. (a) Locations of the 20 observation sites G01–G20 (squares). Six observation sites of the Japan Coast Guard are shown together (triangles). Three types of array configuration with three, four, or six PXPs are indicated by color. (b) One hundred twenty-four campaigns conducted at sites G01–G20 during Cruises #1–12 from September 2012 to September 2016. The array positioning analysis considering gradient was applied to 101 campaigns (light-green circles). (c) Analysis flow. See main text for the detail. NTD = nadir total delay; PXprecision acoustic transponder.

Reference Frame 2008 (Altamimi et al., 2011) was used as the coordinate system of a reference onshore GPS station. The ship attitude was measured by using an equipped fiber-optic or ring-laser gyro in Cruises #6, #8, #11, and #12 or a GPS gyro in the other cruises. The attitude data were finally resampled at 2 Hz in accordance with the GPS sampling rate. The acoustic ranging was executed at intervals of 30 or 60 s during the campaign period, which typically continued for 10–15 hr. The length and carrier frequency of the acoustic signal were 25 ms and 10 kHz, respectively. By calculating the cross correlation between the transmitted and received signals, the round-trip travel times were determined at an accuracy of 10 μs.

In our former studies (Tomita et al., 2015, 2017), the following approach developed by the Scripps Institution of Oceanography (Spiess, 1985; Spiess et al., 1998) was adopted: Once the array geometry is roughly determined, then fixed-point surveys above the array center are conducted repeatedly on a campaign basis to determine the horizontal array displacements. Accordingly, although the moving survey was actually conducted during more than one campaign at individual sites, moving survey data of only a certain campaign were utilized to determine the array geometry. By contrast, all available data of both moving and fixed-point surveys were employed in this study to determine the array geometry and array displacements by using a revised analysis scheme known as multiple campaign analysis (Honsho & Kido, 2017). As a result, the total amount of travel time data was revised to ~1.5 times that reported by Tomita et al. (2017), and the accuracy of the array geometry was greatly improved.

2.3. Sound Speed Profile

Reference vertical profiles of the sound speed, which are referred to as $v_0(z)$ in the following section, were obtained from oceanographic observation data collected during the individual campaigns. This is another difference from Tomita et al. (2017), in which a sound speed profile was prepared for each site based on an open climatological database, World Ocean Atlas 2013 (Locarnini et al., 2013; Zweng et al., 2013) and was used commonly for all campaigns at the site. Small differences in the reference profiles generally have no effect on the results of the array positioning as long as the Scripps Institution of Oceanography approach is adopted. However, reference profiles can have a significant effect when analyzing travel time data with various emission angles collected during moving surveys (Watanabe, 2016).

The sound speed in seawater depends on the temperature, practical salinity, and pressure. Among these factors, the temperature varies significantly with time and place, particularly in shallow parts. We typically conducted one to three expendable bathythermograph casts for each campaign, whereby the temperature to a depth of 1,750 m was measured. Conductivity-temperature-depth (CTD) measurements, reaching near the sea bottom, were intensively conducted at most sites during Cruise #11 (Figure 2b); several other expendable CTD (XCTD) or CTD measurements were conducted during earlier cruises. All of these available data were utilized to produce vertical profiles of the sound speed by using the formula given by Wong and Zhu (1995), which is a translated version of the original equation by Chen and Millero (1977) for adopting the temperature scale ITS-90. A single vertical profile of the sound speed was produced for each campaign as follows. First, several available profiles for the shallow part (<1,750 m), which are based on expendable bathythermograph, CTD, and XCTD measurements conducted during a certain campaign, were averaged to produce a mean profile. The profile was then spliced with a CTD- or XCTD-based profile in the deeper part; if no CTD measurements were conducted during a campaign, which was the most common case, the measurements obtained at the same site but during other campaigns were applied. This is reasonable because seasonal variations in temperature are considered to be rather small in the deep part (>~1,200 m; Watanabe & Uchida, 2016). For site G18, the CTD-based profile of a neighboring site, G19, was substituted because CTD measurement has yet to be conducted at this site. Following Honsho and Kido (2017), the sound speed was reduced by 0.06% prior to use in the analysis because the speed calculated with the formula given by Wong and Zhu (1995) is generally faster than that inferred from GPS-A observations.

3. Analysis Methods

3.1. Overview

The analysis flow is shown in Figure 2c. First, two types of analysis were conducted to determine (1) the position of the transducer relative to the GPS antenna, hereafter referred to as the TR-ANT offset, for each cruise and (2) the array geometry and rigid displacements of the array at the time of campaigns for each site, which is also known as multiple campaign analysis (Honsho & Kido, 2017). A horizontally stratified structure was assumed for the sound speed in these analyses. The TR-ANT offset should be determined for each cruise because different measurement systems and vessels were used. For the TR-ANT offset analysis, data from all campaigns conducted during a cruise were used together, as indicated by the vertical blue lines in Figure 2b. By using the TR-ANT offset values obtained, the geometry of the array and its displacements were determined simultaneously for each site by using data from all campaigns conducted at the site, as shown by horizontal red lines in the figure. The obtained array geometries were then used for the second TR-ANT offset analysis to renew the TR-ANT offset values. The two analyses were repeated until the solutions did not change, although in actuality, a single repetition is sufficient to achieve convergence. Next, array positioning analysis considering the sloping sound speed structure (horizontal gradient of sound speed structure) was conducted for each campaign to reevaluate the array displacements.

In this section, we focus on the theory of array positioning by considering the sloping sound speed structure and its application to the actual data. Honsho and Kido (2017) presented the basic aspects of the analyses assuming a horizontally stratified sound speed structure. A supplemental description of the TR-ANT offset analysis is provided in the supporting information in the present study (Text S1).

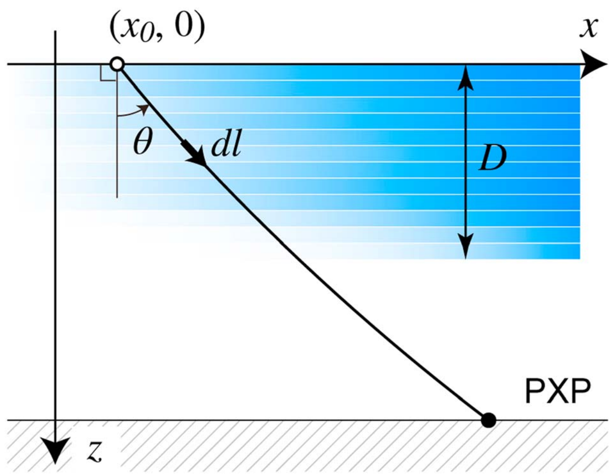

Figure 3. Schematic drawing of an acoustic path in a 2-D space traveling through a sloping sound speed structure. PXprecision acoustic transponder.

3.2. Travel Time Delay Arising From Sloping Sound Speed Structure

We first introduce slowness, which is useful for describing the travel time delay caused by perturbation of the sound speed. Slowness is defined as a reciprocal of the speed, namely, $s = 1/v$; thus, its perturbation is defined as

$$\delta s = 1/(v + \delta v) - 1/v, \tag{1}$$

where v and δv are the sound speed and its perturbation, respectively. Because the perturbation in slowness represents the delay in travel time per unit length arising from δv, the travel time delay can be obtained by integrating δs along the acoustic path as

$$\delta T = \int \delta s \mathrm{d}l. \tag{2}$$

We begin with an acoustic path in a 2-D space (Figure 3). The sound speed is assumed to fluctuate slightly with time and space by $\delta v(x,z,t)$ with respect to a steady, horizontally stratified structure $v_0(z)$. We represent the sloping sound speed structure through a perturbation in slowness, which increases linearly with the horizontal coordinate x at each depth z:

$$\delta s(x, z, t) = \delta s(0, z, t) + \delta s_x(z, t)\, x. \tag{3}$$

Approximating the acoustic path within the velocity fluctuating layer as a straight line, the path is expressed as

$$x = x_0 + z\ \tan\theta, \tag{4}$$

where x_0 and θ indicate the position of the observation and the signed emission angle, that is, the signed nadir angle of the path measured from the downward direction to the positive x axis, respectively (Figure 3). We confirmed by numerical experiments that the error in travel time delay arising from the straight path approximation was expected to be small enough (<3 μs), which is insignificant compared to the observation accuracy of travel time in our case (10 μs), in case δs was uniform with depth. In order to verify the approximation, the angle θ needs to be determined appropriately, as will be explained later in section 3.3.1. By substituting equations (3) and (4) into (2) and using $\mathrm{d}l = \mathrm{d}z/\cos\theta$, we obtain

$$\delta T^{\mathrm{vert}} \equiv \delta T\ \cos\theta = c_0(t) + g(t)\, x_0 + w(t)\ \tan\theta \tag{5}$$

with

$$c_0(t) = \int_0^D \delta s(0, z, t)\mathrm{d}z, \tag{6}$$

$$g(t) = \int_0^D \delta s_x(z, t)\mathrm{d}z, \tag{7}$$

$$w(t) = \int_0^D \delta s_x(z, t) z\, \mathrm{d}z, \tag{8}$$

where D is the bottom depth of the velocity fluctuating layer, in which $\delta s \neq 0$. The effect of an arbitrary depth-distributed sloping structure of the slowness, expressed by equation (3), can be concisely described by only the three quantities, which are integrals of its level and gradient along with the depth rather than their detailed distributions. We call c_0, g, and w the uniform nadir total delay (NTD; Honsho & Kido, 2017), the NTD gradient, and the directional NTD, respectively. Among them, g and w both represent the contribution of the gradient δs_x to the travel times, although their effects on the array positioning are essentially different. The NTD gradient (g) causes a delay associated with the position of the ship (equation (5)), which is a common delay among the travel times for PXPs acquired by ranging at the same time and observation point. Therefore, neither g nor c_0 causes such errors shown in Figure 1. Instead, directional NTD (w) provides different delays between the PXPs, thereby affecting the array positions. We typically use a single

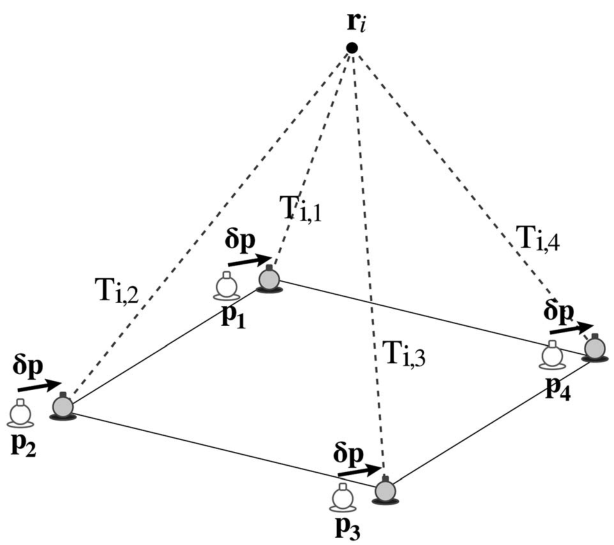

Figure 4. Illustration of ranging at time t_i in a four-precision acoustic transponder array. The example indicates the quantities in the observation equation (14).

vessel for observations and thus have only one observation point at each point in time. Therefore, we cannot separate the contributions of $c_0(t)$ and $g(t)$ in practice. In this context, we may newly define the sum of the first and second terms in equation (5) as $c(t)$, which we refer to herein as the on-the-spot NTD. Thus, equation 5 can be rewritten as

$$\delta T^{\text{vert}} = c(t) + w(t)\ \tan\theta. \tag{9}$$

This formulation is essentially the same as that previously presented by Kido et al. (2007), which is a modified version of the formulation given by Kido (2007). Kido (2007) showed that equation (9) is valid also for the case boundary surfaces between layers of different slowness are inclined. Kido (2007) clarified that only the directional NTD (w) is crucial for array positioning, and the present study additionally shows that the formulation is still valid for a more generalized sloping structure and clarifies the physical meanings of c and w. We also note that g and w in equation (5) correspond to what are referred to as "first-order gradient" and "second-order gradient" by Yokota et al. (2018a).

In a 3-D space, the sloping structure of the slowness perturbation represented by equation (3) is rewritten as

$$\delta s(x, y, z, t) = \delta s(0, 0, z, t) + \delta s_x(z, t)\, x + \delta s_y(z, t)\, y, \tag{10}$$

and equation (9) becomes

$$\delta T^{\text{vert}} = c(t) + \mathbf{w}(t)\cdot\widehat{\mathbf{h}} \tag{11}$$

with

$$\mathbf{w}(t) = \left(\int_0^D \delta s_x(z, t) z\, \mathrm{d}z, \int_0^D \delta s_y(z, t) z\, \mathrm{d}z\right), \tag{12}$$

$$\widehat{\mathbf{h}} = (\tan\theta \sin\alpha,\ \tan\theta \cos\alpha), \tag{13}$$

where θ and α indicate an unsigned angle from the vertical direction and an azimuth of the acoustic path, respectively. Although $\mathbf{w}$ as well as c should vary with time in actuality, we treat $\mathbf{w}$ as unchanging because it is a bias remaining after averaging over the observation time and has a significant effect on the array positioning, as previously mentioned. Therefore, the effect of the sloping sound speed structure is now represented by a time-invariant 2-D vector $\mathbf{w}$.

3.3. Array Positioning Considering Sloping Sound Speed Structure

3.3.1. Observation Equation

Array positioning is an analysis technique used to determine array displacement assuming that the relative positions between PXPs are unchanged, that is, the array moves rigidly (e.g., Spiess et al., 1998). In array positioning that assumes a horizontally stratified sound speed structure, the array displacement and time fluctuations of the sound speed during each campaign are determined for the given initial positions of the PXPs as unchanging array geometry and the reference depth profile of the sound speed. To incorporate the gradient effect in the array positioning, an additional term was added to the right side of the conventional observation equation assuming horizontal stratification (equation 3 in Honsho & Kido, 2017), as

$$\xi_{i,k} T_{i,k} = \xi_{i,k} f(\delta\mathbf{p}; \mathbf{r}_i, \mathbf{p}_k, v_0(z)) + c(t_i) + \mathbf{w}\cdot\widehat{\mathbf{h}}_{i,k}, \tag{14}$$

where $T_{i,k}$ is the observed travel time to the kth PXP acquired by the ith shot at time t_i, $\delta\mathbf{p}$ is rigid array displacement, $\mathbf{r}_i$ is a transducer position at time t_i, and $\mathbf{p}_k$ is the initial position of the kth PXP as determined previously in the multiple campaign analysis (Figure 4). Function f produces the round-trip travel time through ray tracing between a transducer and a PXP positioned at $\mathbf{r}_i$ and $\mathbf{p}_k + \delta\mathbf{p}$, respectively, assuming

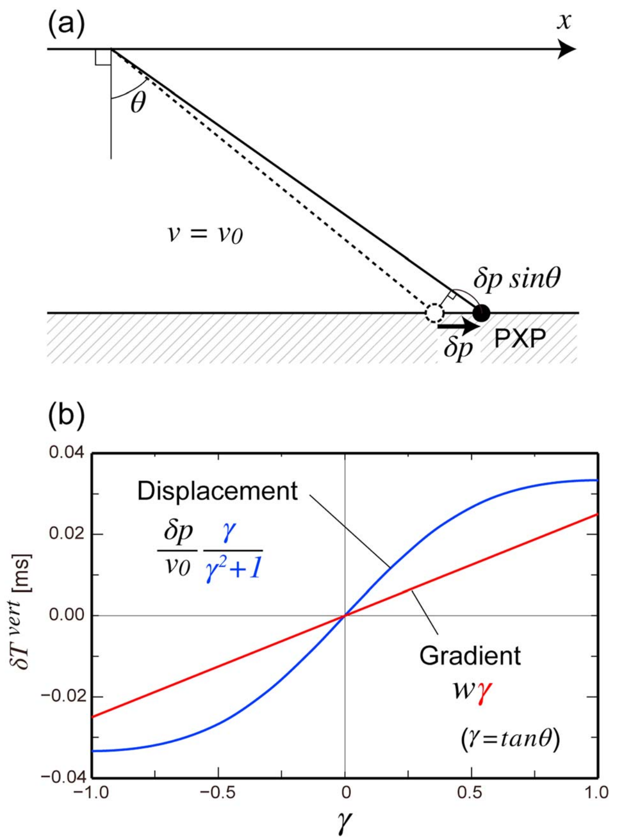

Figure 5. Effects of PXP displacement and sloping sound speed structure on travel time in a 2-D space. (a) Schematic drawing showing a change in slant range by a slight PXP displacement. (b) Comparison of the two effects. Changes in vertically normalized travel time are plotted against $\gamma = \tan\theta$. PXprecision acoustic transponder.

a horizontally stratified sound speed structure $v_0(z)$. The coefficient $\xi_{i,k}$ is a scaling factor used to normalize the travel time in the vertical direction according to the slant of the path in the fluctuating layer. The scaling factor is defined as the ratio of the synthetic travel time along a vertical path to the depth D, the assumed bottom depth of the fluctuating layer, to that along the raypath, that is, $\xi = T_D^{vert}/T_D$ (Honsho & Kido, 2017). Accordingly, the tangent in equation (13) is given as $\sqrt{(1-\xi^2)/\xi^2}$ in the actual calculation by regarding ξ as the cosine. Note that the directional NTD ($\mathbf{w}$) is now defined to produce a delay of a round-trip travel time, it corresponds to the double value of $\mathbf{w}$ defined regarding a one-way travel time in equation (11). The time variation of the on-the-spot NTD, $c(t)$, is represented through the superposition of a finite number of basis functions as $c(t) = \sum_{m=1}^{M} a_m \Phi_m(t)$. In the actual calculation, cubic B-splines were used for basis functions and distributed at 250-s intervals over the time length of individual campaigns. The model parameters to be determined are then the array displacement $\delta\mathbf{p}$ (a 3-D vector), directional NTD ($\mathbf{w}$, a 2-D vector), and expansion coefficients a_m ($m = 1, \ldots, M$).

3.3.2. Separation of Array Displacement and Gradient

The simple example shown in Figure 1 indicates that the array displacement cannot be distinguished from the gradient, that is, $\delta\mathbf{p}$ cannot be separated from $\mathbf{w}$ in some cases. In this section, we consider the data requirements for the separation of the two quantities. We begin with a 2-D case again and assume the sound speed to be uniform (v_0) for simplicity. If a PXP is displaced slightly by δp (Figure 5a), the travel time changes by approximately $\delta p \sin\theta/v_0$, and its vertically normalized quantity becomes

$$\delta T^{\mathrm{vert}} \approx \frac{\delta p \sin\theta \cos\theta}{v_0} = \frac{\delta p}{v_0}\frac{\gamma}{\gamma^2+1}, \tag{15}$$

where $\gamma \equiv \tan\theta$. On the contrary, if the sound speed has a sloping structure, it causes a vertically normalized travel time delay of $\delta T^{\mathrm{vert}} = w\gamma$, as indicated in equation (9). The delays in the vertically normalized travel time arising from these two factors are compared in Figure 5b. The figure shows that the effects of the displacement and gradient on travel times, although somewhat different, are quite similar. In particular, when the PXP is located near the observation point (γ~0), the effect of displacement (blue line) is approximately proportional to γ and thus cannot be distinguished from that of the gradient (red line). It is clear that ranging data with at least two different, nonzero$|\gamma|$, that is, two different, nonzero emission angles, are needed to distinguish the two effects. This indicates that the travel time data collected during a point survey at the center of a three-PXP equilateral triangle array or a four-PXP square array have little information for the separation of the array displacement and gradient because they have nearly the same emission angles, as shown by the array configurations in the Figure 2a inset. For these sites, moving surveys are therefore indispensable for acquiring ranging data with various emission angles for solving the gradient. For the six-PXP sites, however, the separation is possible even without a moving survey because the array is configured such that the three inner and three outer PXPs are positioned at different distances from the center.

3.3.3. Constraint From NTD Gradient

We determined that the array displacement and gradient are distinguishable in principle if a suitable data set is used. However, both experiments using actual data and numerical tests revealed that the problems of poor determination or significant misinterpretation of the gradient can occur under certain circumstances. The former problem likely arises when the data are insufficient in quantity and quality for reducing random errors to a sufficient level to resolve the array displacement and gradient. This often occurs for the three- or four-PXP arrays because the data collected during a fixed-point survey at the array center, which generally outweigh the amount of data obtained during a moving survey to a significant degree, have little information

10.1029/2018JB017135

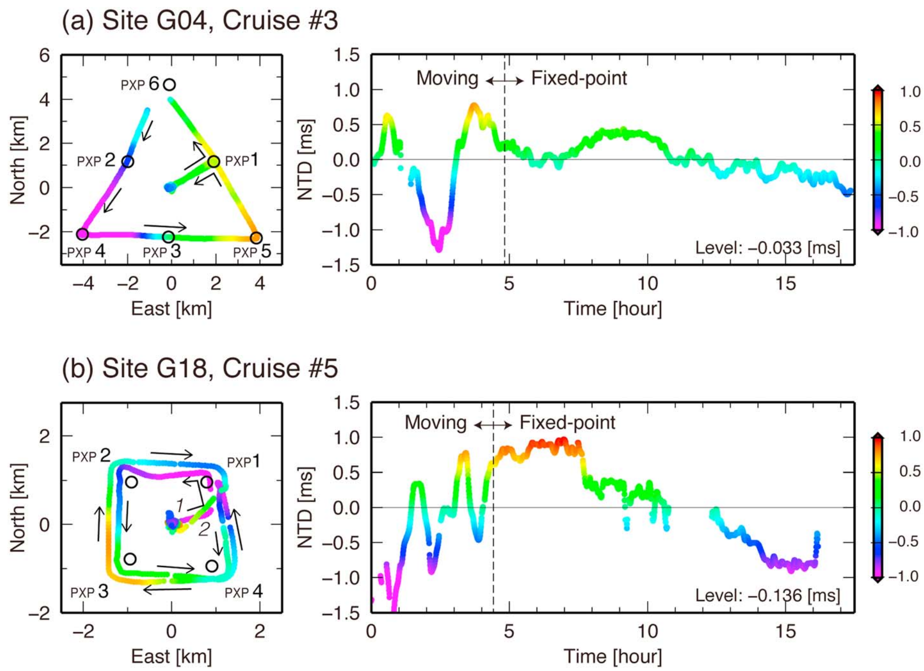

Figure 6. Examples of the variations of the on-the-spot NTD during campaigns of Cruise #3 in a six-PXP site G04 (a) and of Cruise #5 in a four-PXP site G18. NTD = nadir total delay; PXprecision acoustic transponder.

for resolving the two quantities. The problem appears tangibly in the analysis results as large estimation errors. The latter problem, misinterpretation of the sound speed gradient, can occur because the solution is relatively easily influenced by model error, that is, deviation of the actual horizontal variation from the assumed linear variation. This problem can arise even in six-PXP arrays for which fixed-point survey data are as informative as moving survey data. In contrast to the former problem, the latter tends to result in systematic estimation errors and thus does not clearly appear in the analysis results. Numerical tests revealed that even horizontal variations of the sound speed that are flat as a first-order approximation can be misinterpreted as having a certain gradient, thereby causing significant errors in the estimates of the array displacement. This misinterpretation can intrinsically arise because the number of PXPs, which is six at most, is insufficient in certain cases for properly approximating the actual horizontal variations in the sound speed as linear variations.

To resolve these problems, we employed the information of the NTD gradient. Figure 6a shows on-the-spot NTDs during a campaign obtained from the analyses assuming horizontal stratification that were plotted against time (right panel) or on a map along the ship tracks (left panel). Although all of these variations were assumed to be temporal, a clear spatial trend appeared such that the NTD was lower in the west and higher in the east. In addition, the amplitude of the NTD variations was significantly greater during the moving survey than that during the fixed-point survey. This suggests that a considerable portion of the variations that occurred during the moving survey may actually be spatial variations caused by the ship's movement in a field having a persistent NTD gradient. For example, a positive eastward NTD gradient is strongly implied for the case of Figure 6a. In principle, the NTD gradient (g) and the directional NTD (w), defined by equations (7) and (8), respectively, are independent quantities. However, they are related if the depth distribution of the gradient is specified. If the gradient of the slowness perturbation is assumed to be uniform with depth, that is, if $\delta s_x(z)$ in equations (7) and (8) is a constant, it can be immediately derived that

$$w = (D/2)\, g. \tag{16}$$

By using the above relationship and assuming a particular value for D, we can obtain an estimate of w through g, which can be determined to a certain degree from the spatial distribution of the on-the-spot NTD during a moving survey. The assumption of a uniform gradient with depth may greatly impair the generality of the sloping sound speed structure. However, given that our data are only somewhat capable of determining w, we adopted this as an appropriate and practical measure for a more robust determination. Yasuda et al. (2017) adopted essentially the same measures and utilized variations in the travel time delay associated with the ship movement for determination of w.

Substituting equation (16) into equation (14), we can rewrite the observation equation as

$$\xi_{i,k} T_{i,k} = \xi_{i,k} f(\boldsymbol{\delta}\mathbf{p}; \mathbf{r}_i, \mathbf{p}_k, v_0(z)) + c_0(t_i) + \mathbf{g}\cdot\mathbf{h}_{i,k}, \tag{17}$$

with

$$\mathbf{h}_{i,k} = \left(r_{i\_x}, r_{i\_y}\right) + (D/2)\,\widehat{\mathbf{h}}_{i,k}, \tag{18}$$

where (r_{i-x}, r_{i-y}) is a 2-D vector of the horizontal components of $\mathbf{r}_i$. Then, to discriminate the combined effect of the NTD gradient and the ship's movement from the true time variations of the uniform NTD, $c_0(t)$, we impose a constraint that $c_0(t)$ is small to a certain degree. Representing $c_0(t)$ by the superposition of basis functions as $c_0(t) = \sum_{m=1}^{M} a_m \Phi_m(t)$, the constraint is expressed as

$$a_m = 0 \quad (m = 1, \ldots, M). \tag{19}$$

As the constraint becomes stronger, large on-the-spot NTD variations that occur during moving surveys (Figure 6a) need to be considered as spatial variations caused by the NTD gradient and the ship's movement rather than time variations of the uniform NTD. The optimal strength of the constraint was determined by using Akaike's Bayesian information criterion (Akaike, 1980) calculated by using the algorithm of Yabuki and Matsu'ura (1992). We provide further descriptions on applying the method to actual data in the supporting information (Text S2). However, it should be noted here that the solution now becomes dependent on the assumption of D (the bottom depth of the fluctuating layer) to a certain degree because the directional NTD (w) is now related to the NTD gradient (g) through D (equation (16)). We finally assumed D to be 500 m, although the results did not change significantly at D = 1,000 m, as shown also in the supporting information (Text S2 and Figures S3 and S4).

Yasuda et al. (2017) and Yokota et al. (2018a) both took a step-by-step approach in which the unknowns in the problem, such as the array or PXP position, temporal variation of the sound speed, and horizontal gradient of the sound speed, are determined individually in each step. With this approach, however, a certain solution can be obtained even for indefinite problems. By contrast, we solved them at once using the observation equation including all the unknowns, as shown in equation (14) or (17), thereby clarifying the trade-off between the model parameters and how it was resolved.

4. Results

4.1. Horizontal Gradient

The magnitude of the NTD gradient,$|\mathbf{g}|$, obtained from the 101 campaigns to which the gradient analysis was applied ranged from 0.01 to 0.45 ms/km or was 0.12 ms/km in the mean. The gradient had various azimuth and magnitude among the campaigns and exhibited neither a clear seasonal nor spatial trend. Changes in the array position brought by the consideration of the gradient ranged from 0.3 to 11.0 cm, or was 3.1 cm in the mean, in horizontal distance. As explained in section 3.3.2, it is expected that the gradient (g) and array displacement (δp) has a trade-off with each other. From equations (9), (15), and (16), they are approximately related as

$$2\frac{\delta p}{v_0}\frac{\gamma}{\gamma^2+1} \approx w\gamma = \frac{Dg}{2}\,\gamma, \tag{20}$$

where $\gamma \equiv \tan\theta$. Note that the factor 2 on the left side is required here because the NTD gradient (g) was defined in actual application as to cause delay in round-trip travel time. Using the relationship and the most common value of γ ~ 0.5 (θ ~ 27°) in our observations, a change of the array position caused by the mean gradient 0.12 ms/km can be estimated to be ~2.8 cm, which is in good agreement with the above mean of array position changes (3.1 cm). The NTD gradients and array position changes are plotted together in

Figure S5 in the supporting information. The figure shows, as expected, that the array positions moved in the nearly opposite direction of the gradient. The estimation errors of the NTD gradient and the array position were 0.02 ms/km and 0.6 cm in the mean, each of which affects vertically normalized travel time nearly equally by ~3 μs.

The NTD gradient of 0.12 ms/km approximately corresponds to a uniform gradient of the sound speed of 0.27 m/s/km within the surface layer to the depth D = 500 m, as calculated through the relationship $g = 2D/(v+1 \times g_v) - 2D/v \sim -2Dg_v/v^2$, where v and g_v represents the sound speed and its gradient, and assuming v = 1,500 m/s. Yokota et al. (2018a) observed a sound speed gradient of ~0.07 m/s/km for one of the GPS-A benchmarks of the Japan Coast Guard (JCG), called HYG2, which is ~1,900 m in water depth and located in the region of the Kuroshio, which is a strong warm ocean current running off the southern coast of Japan. The value of the sound speed gradient was estimated assuming a uniform gradient over the entire depth. Because travel time delay arising from the sound speed gradient increases with the square of the depth to which the gradient is present, the sound speed gradient of 0.07 m/s/km estimated for the depth of 1,900 m corresponds to that of $0.07 \times (1{,}900/500)^2 \sim 1$ m/s/km in a 500 m-thick layer. This value is about 4 times the mean gradient and close to the maximum gradient obtained in this study.

4.2. Array Displacement

The array displacements ultimately obtained are shown as red circles in Figure 7; the previous results of Tomita et al. (2017) are shown as black circles. Their values are given in Table S1 in the supporting information. For the 23 campaigns excluded from the gradient analysis, as indicated by gray-filled circles in Figure 2 b, we adopted the results from multiple campaign analysis assuming a horizontally stratified sound speed structure. Coseismic steps caused by the two successive aftershocks (Mw7.2 for each) on 7 December 2012 have been corrected for sites G10–G12, G14, and G16; the original data are given in Table S2 in the supporting information of Tomita et al. (2017). The array positions at individual campaigns were first modified from the previous results of Tomita et al. (2017) through revision of the analysis scheme, via adaptation of the multiple campaign analysis (Honsho & Kido, 2017), by 0.6–11.7 cm in horizontal distance or 5.4 cm in the mean. Then, as previously explained in section 4.1, the data were further modified by 0.3–11.0 cm, or 3.1 cm in the mean, by applying the positioning method considering the gradient. The two modifications are shown individually in Figure S6 and explained in detail in Text S3 in the supporting information. These results indicate that the impact of the two modifications in the analysis method differs among the campaigns and that both of them made significant contribution to the revision of array positions. Finally, the total differences in array position from the previous results amounted to 0.2–15.8 cm or 6.0 cm in the mean.

4.3. Displacement Rate

It is expected that the movements at the sites can be primarily approximated as steady linear motion because the observation period does not include the initial fast transient during the first year after the mainshock. We then applied weighted least squares linear fitting for estimating the displacement rates throughout the observation period for individual sites. For sites G09–G12, the array positions recorded before 2013 were not utilized because it appears that nontectonic movements might be superimposed over these sites during the early period (Text S4 and Figure S7 in the supporting information). Estimation errors of horizontal array positions calculated in the analysis considering the gradient are generally larger than those in the analysis assuming horizontal stratification. Larger estimation errors mainly result from the trade-off between the gradient and array position. Because estimation errors do not contain possible systematic errors arising from model error, this situation does not mean that the array positions obtained considering the gradient are less reliable than those obtained assuming horizontal stratification. Therefore, the estimation errors of the array positions of the 23 campaigns excluded from the gradient analysis were deliberately doubled before being utilized for the weighted least squares fitting to avoid giving them an unreasonably high weight. Figure 7 shows the resulting fitted lines as light-red lines, along with the value of their rates. For mapping the crustal deformation, the velocity of the North American plate, which was calculated for each site based on NNR-MORVEL56 (Argus et al., 2011), was subtracted from the displacement rates in the International Terrestrial Reference Frame 2008 frame. The resulting displacement rates relative to the North American plate, ranging from 2.4 to 13.8 cm/year, are plotted as vectors in Figure 8a and are given in Table S2 in the supporting information. The displacement rates for the six benchmarks of the JCG, calculated from

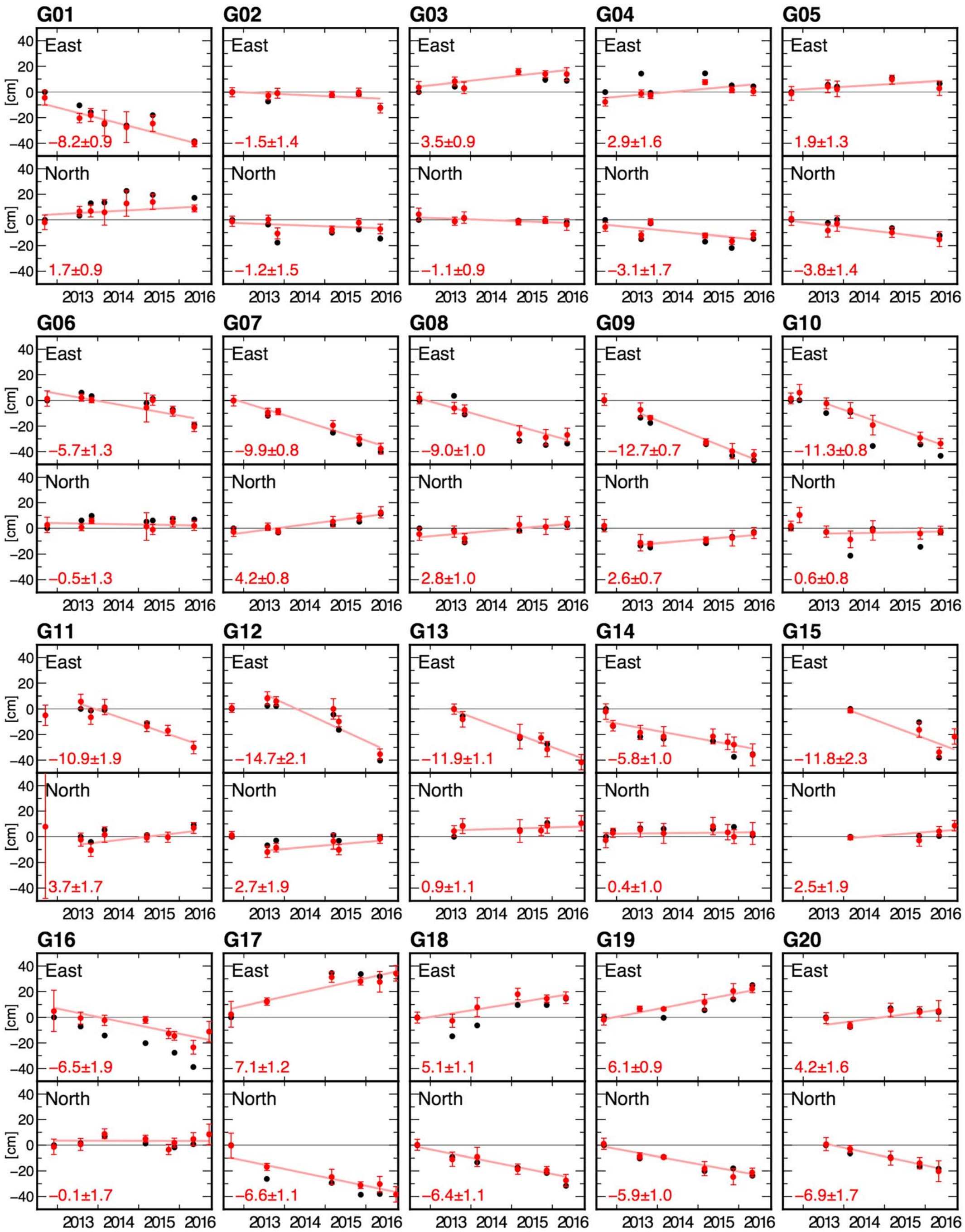

Figure 7. Array displacements estimated for sites G01–G20. Upper and lower panels of each sites show eastward and northward displacement, respectively. Red and black colors indicate the results of this study and those of Tomita et al. (2017), respectively. Error bars of this study (red) show 10-times estimation errors. The results of linear regression are shown by light-red lines; the value of their rates in units of centimeters per year.

the published data of the array positions (Yokota et al., 2018b; Figure S8 in the supporting information) for nearly the same period as that of our observations, are shown as gray arrows in Figures 8a and 8b.

4.4. Comparison With Previous Results

The horizontal displacement rates show along-trench variations that are generally similar to the previous results of Tomita et al. (2017); Figure 8b). The displacement rate is small in the northern area including G02–G05; large and landward in the middle area including G06–G16, where large coseismic slip occurred

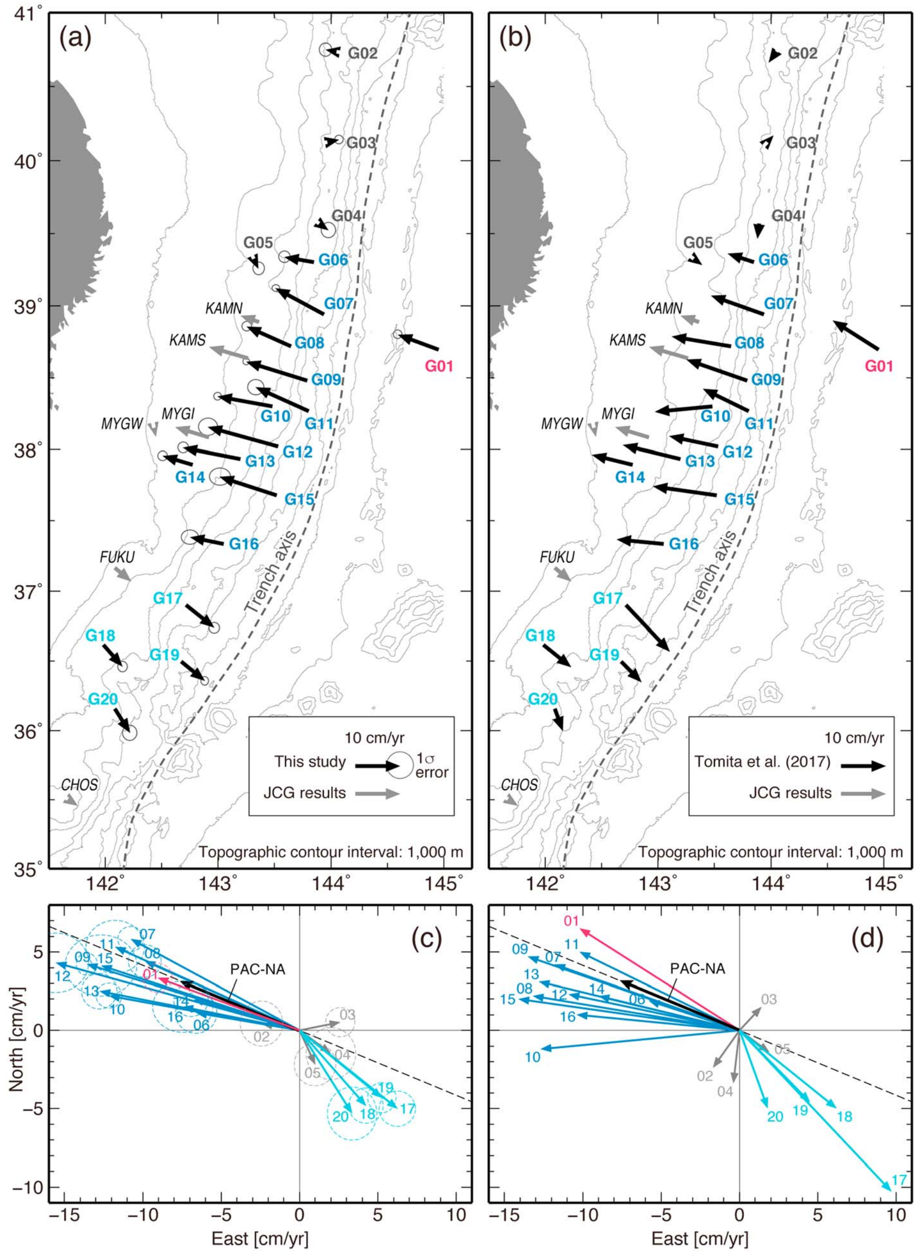

Figure 8. Horizontal displacement rates relative to the North American plate including the results of (a) and (c) this study and (b) and (d) those of Tomita et al. (2017). The results from the six JCG sites are shown together in (a) and (b) by gray arrows. The black arrow in (c) and (d) indicates the velocity of the Pacific plate relative to the North American plate (PAC-NA). JCG = Japan Coast Guard.

during the 2011 Tohoku earthquake; and seaward in the southern area including G17–G20. However, some improvements from the previous results can be recognized: The landward vectors in the middle area in this study (dark-blue arrows in Figure 8c) are more similar in direction than those in the previous study (Figure 8d). Regarding the seaward vectors in the southern area (light-blue arrows in Figures 8c and 8d), the extremely high speed of site G17 in the previous study was reduced to be comparable to that of the other three sites G18–G20. Considering that the major sources of displacement in the observation period are viscoelastic relaxation and afterslip of the 2011 Tohoku earthquake (e.g., Hu et al., 2016; Tomita, 2018; Wang et al., 2018), the deformation scale should be larger than the separation of the GPS-A sites (30–40 km). Therefore, the movement is unlikely to vary largely between neighboring sites, and we consider that the increased similarity in direction and rate between neighboring sites suggests the enhanced accuracy of the

10.1029/2018JB017135

array positions. The results also indicate that the direction of the landward (seaward) vector is counterclockwise (clockwise) from the relative plate motion direction (Figure 8c) and thereby are approximately normal to the local strike of the trench axis. The array displacements obtained in this study (red circles in Figure 7) still contain unnatural motion for actual crustal movement, indicating that errors have yet to be completely removed. We suspect that these remaining errors are attributed mainly to the horizontal heterogeneity of the sound speed in the deep parts, which can have a significant effect on array positioning despite its relative smallness (Matsui et al., 2018). Nevertheless, the improvements mentioned above suggest that the accuracy of the array positions was enhanced to a considerable extent by considering the effect of a sloping structure in the shallow parts as well as by introducing multiple campaign analysis.

The three JCG sites in the middle part, KAMN, KAMNS, and MYGI, have nearly the same directions, which fall within the variation of landward movement of our sites. The most landward JCG site, MYGW, is moving in a different direction at a significantly smaller rate, indicating a hinge line of the systematic seaward movement observed at the onshore Global Navigation Satellite System sites (e.g., Ozawa et al., 2012; Suito, 2017; Yamagiwa et al., 2015). The two southern JCG sites, FUKU and CHOS, are directed seaward in agreement with our results, although the movement is at smaller rates than those of G17–G20. This indicates that the seaward motion declines as southward as well as landward.

5. Discussion

5.1. Site on the Pacific Plate

Site G01 is only the benchmark on the incoming Pacific plate, located ~100 km northeast of the main rupture zone. Movement at this site is of significant importance in evaluating viscoelastic relaxation because it is little affected by the uncertain state of the plate interface. The estimated horizontal displacement rate of G01, at 18.0 cm/year, was significantly larger than the relative motion of the Pacific plate (8.3 cm/year), when the first five campaigns were completed (Tomita et al., 2015). This suggests a significant contribution of viscoelastic relaxation. However, the result was revised down to 12.1 cm/year after two more campaigns (Tomita et al., 2017). This may indicate deceleration of the postseismic deformation at G01, although our observation was infrequent and too brief in total period to confirm it. The velocity was further reduced to 9.7 cm/year in the present study (pink arrow in Figure 8c), which has now become comparable to the relative plate motion (black arrow), 8.3 cm/year in the N68°W direction (MORVEL; DeMets et al., 2010). If the assumed plate motion is true, the effect of viscoelastic relaxation has been relatively small at this site during our observation period, at 1–2 cm/year. The present viscoelastic relaxation model of Sun et al. (2014) predicts a relatively large displacement rate of ~6 cm/year for this site (Figure 2 in Tomita et al., 2017). Our results can help to estimate more practical values of the rheological properties of the viscoelastic medium, particularly those of the oceanic mantle and the lithosphere-asthenosphere boundary.

5.2. Middle Area

The remarkable landward movements in the middle area are attributed primarily to viscoelastic relaxation of stress induced by the large coseismic slip. Many studies have placed importance on the effect of viscoelastic relaxation and incorporated this effect in the modeling of postseismic deformation of the 2011 Tohoku earthquake (e.g., Hu et al., 2016; Suito, 2017; Sun et al., 2014; Tomita, 2018; Wang et al., 2018; Yamagiwa et al., 2015). Viscoelastic relaxation is mainly controlled by the rheological structure of the viscoelastic medium and the distribution of coseismic slip. As with Site G01, movement at the sites above the main rupture zone should provide crucial information on these parameters.

The horizontal displacement rates of G07–G15 in the middle area are significantly larger than the relative motion of the Pacific plate (Figure 8c). This observation alone provides strong evidence of viscoelastic relaxation and the required degree of plate coupling in this region necessary to transmit westward viscoelastic responses in the oceanic mantle to the seafloor on the overriding plate through the plate interface. Therefore, plate subduction should also contribute significantly to the observed movement. In the following discussion, we roughly evaluate the contribution of viscoelastic relaxation to the observed movements assuming full locking conditions. If the fault is not fully locked in actuality, the observed movement should represent a fraction of the sum of movement by the plate subduction and viscoelastic relaxation. However, the following discussion assuming full locking conditions would essentially hold also for a certain high degree of locking conditions.

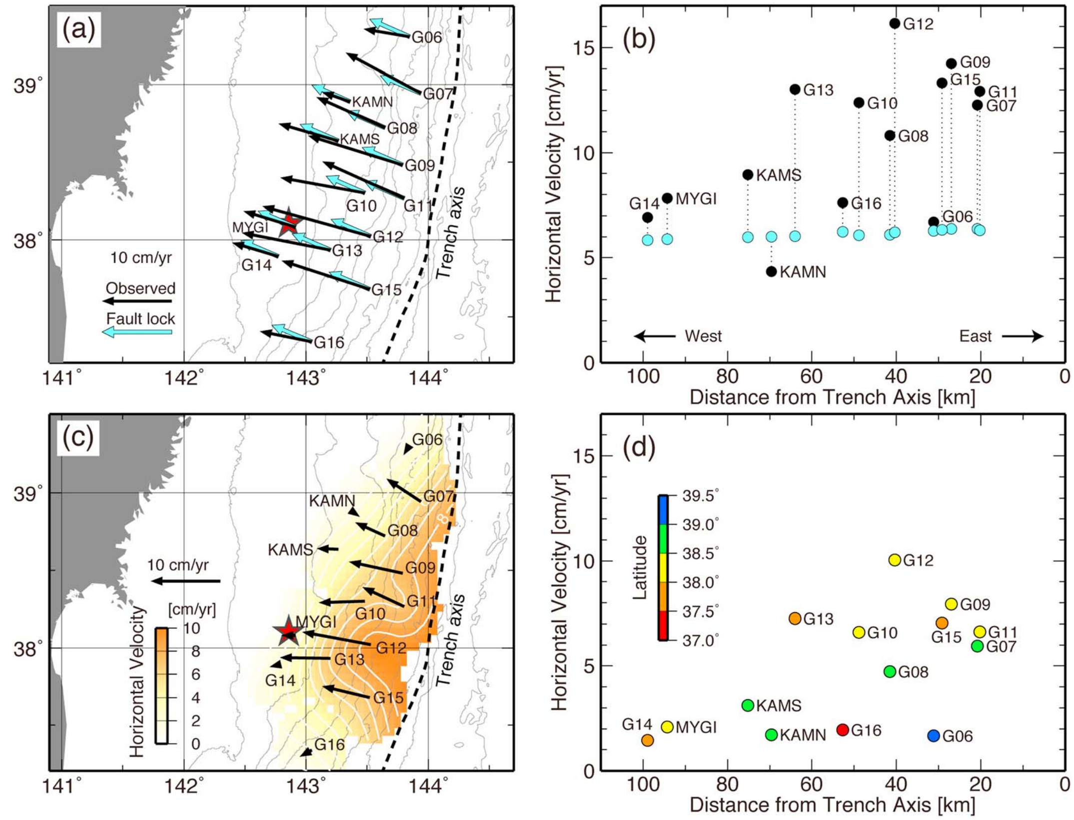

Figure 9. Movement in the middle area. (a) Observed displacement rates (black arrows) and model rates owing to plate subduction that were calculated assuming full fault locking (light-blue arrows). The red star indicates the mainshock hypocenter. (b) Horizontal velocities plotted against the distance from the trench axis. Observed and synthetic values are shown by black and light-blue circles, respectively. (c) Viscoelastic relaxation component under full locking conditions. Color scale and contours show horizontal velocity. (d) Same as (c) but plotted against the distance from the trench axis. Color indicates latitude of the sites.

Figure 9a shows the observed (black arrows) and synthetic movement owing to plate subduction (light-blue arrows), which was calculated assuming full locking of the plate interface and a uniform elastic medium. The formulation of Okada (1992) and the gridded data of the slab geometry (Nakajima & Hasegawa, 2006; Kita et al., 2010, available at http://www.mri-jma.go.jp/Dep/sv/2ken/fhirose/en/en.PlateConfiguration.html) were used in the calculation. The velocities are also plotted against the distance from the trench axis in Figure 9b. We considered simply elastic deformation. However, this may have been inadequate for sites G07, G09, G11, and G15, which are in very close proximity to the trench axis, because they might be located on the deformation prism (Tsuru et al., 2002) or in the tsunamigenic area that was greatly stretched in an inelastic manner during the Tohoku earthquake (Fujii et al., 2011; Tsuji et al., 2013). When the fault is fully locked, subtracting the model displacement owing to plate subduction from the observed value should give the component of viscoelastic relaxation (Figure 9c), because afterslip is expected to have been little occurring in this area. The relative variations in the resulting viscoelastic relaxation component among the sites are essentially the same as those of the observed movement (Figure 9a) because both the observed and model vectors have similar directions, and the model vectors are similar in magnitude (Figure 9b). It is inferred that the viscoelastic relaxation component at the near-trench sites in the main rupture zone, G07–G13 and G15, is ~5–10 cm/year, which is a requirement to be met in viscoelastic relaxation models. In most published studies of viscoelastic relaxation, any degree of decoupling along the plate interface is not taken into account in calculating the viscoelastic relaxation process other than the initial coseismic dislocation context. An exception is the research by Hu et al. (2016), who incorporated a thin viscoelastic shear zone on the shallow part of the plate interface. Therefore, it should be noted that most published models predict motion under full locking conditions.

In the along-trench variation of the viscoelastic relaxation component (Figure 9c), movement of the northernmost and southernmost sites, G06 and G16, respectively, is distinctively small for their relatively small

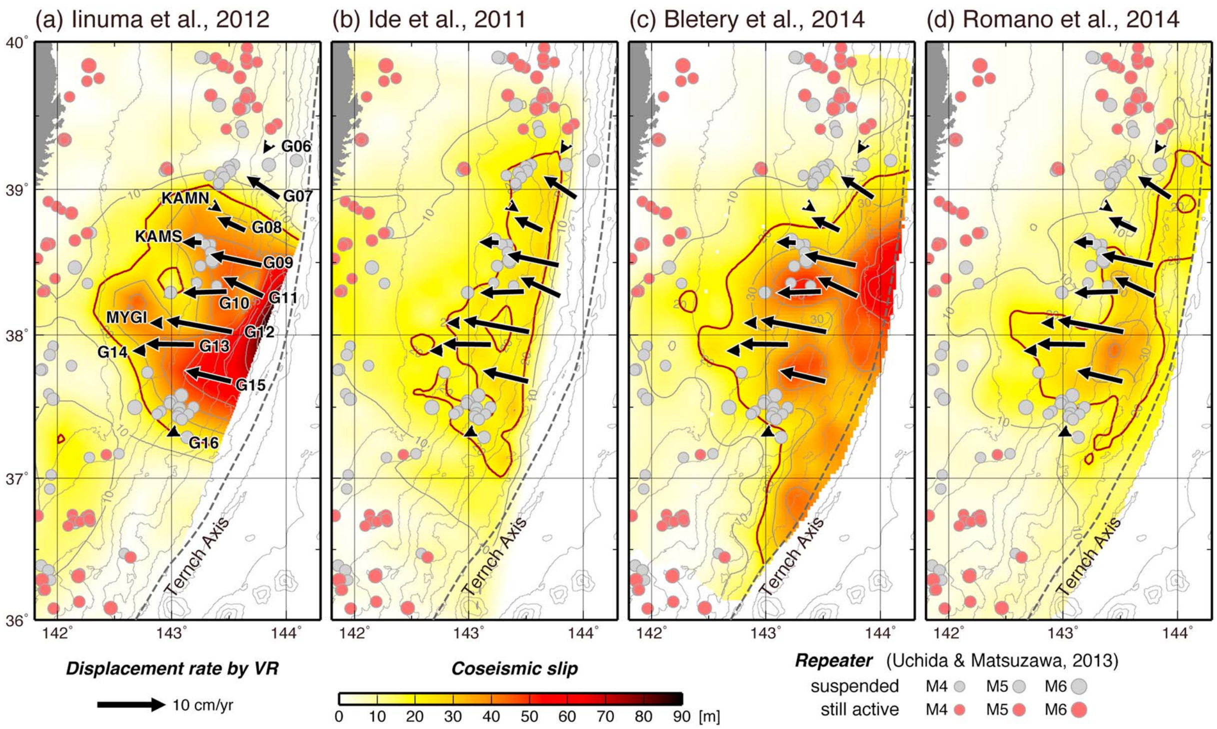

Figure 10. Comparison of the viscoelastic relaxation (VR) component (black arrows; same as those in Figure 9c) with coseismic slip models (color scale and contours) and the epicenter distribution of repeating earthquakes (gray and light-red circles; Uchida & Matsuzawa, 2013). Coseismic slip models of (a) Iinuma et al. (2012), (b) Ide et al. (2011), (c) Bletery et al. (2014), and (d) Romano et al. (2014) are shown. Contours of 20-m coseismic slip are highlighted by bold, dark-red lines. Gray circles indicate repeaters that have been suspended after the 2011 earthquake, and light-red circles indicate currently active repeaters.

distances from the trench axis (Figure 9d) and thus are clearly differentiated from G07–G13 and G15, the other near-trench sites. This result suggests that the northern (southern) limit of such large coseismic slip necessary to drive significant viscoelastic flow is positioned at ~39.2°N (~37.5°N), which is between G06 and G07 (G15 and G16). The inferred extent appears to be in good agreement with large-slip (>~20 m) zones in some existing models of coseismic slip distribution obtained from seismological, seafloor geodetic, and tsunami data (Figure 10). As reported by Tomita et al. (2017), the coseismic slip distribution of Iinuma et al. (2012) lacks the expected large slip near the trench axis to the north of ~38.7°N (Figure 10a). However, the results obtained by incorporating seismological and tsunami data commonly predicted large slip extending north beyond 39°N near the trench (Figures 10b–10d). Uchida and Matsuzawa (2013) reported that repeating earthquakes have completely ceased within the main rupture zone since the Tohoku earthquake. The distribution of those suspended repeaters, shown as gray circles in Figures 10a–10d, also agrees well with our results.

In addition, the along-trench distribution of the viscoelastic relaxation component (Figure 9c) is clearly asymmetric, showing a peak near 38°N, which is the updip of the mainshock hypocenter, and extends much farther to the north than to the south. If we assume that this distribution is attributed primarily to the coseismic slip distribution, it is inferred that another secondary slip patch existed in the north part in addition to the primary slip patch at ~38°N. Hasegawa and Yoshida (2015) reported that this feature of two large slip patches in the south and north areas is commonly recognized in the coseismic slip distribution models that incorporate seafloor geodetic data. Hasegawa and Yoshida (2015) performed stress tensor inversions for events in the footwall after the 2011 Tohoku earthquake. They revealed that largest slip in the northern slip patch reached the trench axis, whereas that in the primary southern patch occurred deeper landward. This is consistent with the results of Sun et al. (2017), who made precise inspection of differential seafloor bathymetry (Fujiwara et al., 2011) and inferred that coseismic slip increases toward the trench axis only slightly (significantly) in the southern (northern) part at ~38°N (~38.8°N). Unfortunately, the spatial resolution of our results from the GPS-A observations is insufficient for confirming the inferred difference of across-axis

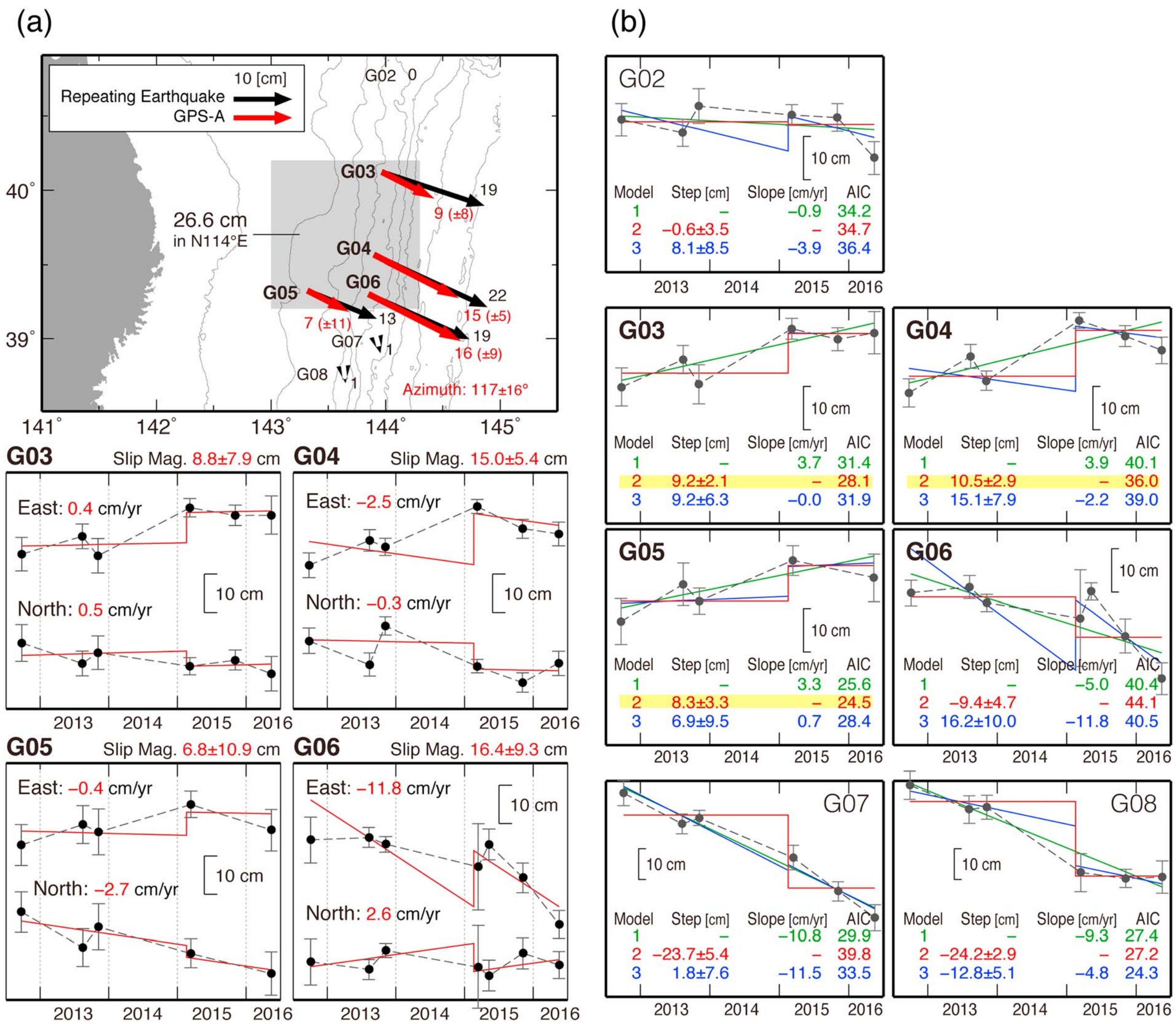

Figure 11. Slow slip event in early 2015 inferred from our GPS-A observations. (a, upper map) Step motions that occurred at CE 2015.1, estimated from repeating earthquake data (black arrows; Uchida et al., 2018) and the results of the present study (red arrows). Those from repeating earthquakes were calculated assuming a 26.6-cm dislocation in the relative plate motion direction (N114°E) along a rectangular fault on the plate interface (gray box). (lower graphs) Results of analysis using the array displacements at sites G03–G06 assuming a common azimuth of the step motion between the sites. The resulting step motions are plotted on the upper map. Error bars indicate 10-times estimation error. (b) Fitting results of three models for the movement in the N114°E direction at sites G02–G08 showing uniform linear motion (green lines), no movement except a step at CE 2015.1 (red lines), and uniform linear motion and a step at CE 2015.1 (blue lines).

patterns of slip distribution between the northern and southern parts. However, it strongly supports the existence of the secondary slip patch near the trench axis in the northern part.

5.3. Northern Area

Sites G02–G05 in the northern area are generally moving slowly at 2.4–2.6 cm/year, which contrasts with the threefold increase in the seaward movement of G17–G20 in the southern area at 6.3–8.0 cm/year. This clear difference in response to the adjacent large earthquake reflects the different frictional and mechanical properties of the plate interface between the northern and southern areas. It has been suggested from repeating earthquake data that the afterslip in the northern area was small and rather episodic. The temporal variation in the slip rate estimated from repeating earthquakes in this region (Uchida et al., 2018) shows an abrupt increase immediately after the 2011 earthquake followed by large variations with a gradual decrease. A steep peak in the slip rate was found in early 2015, suggesting an episodic slow slip event (SSE) on a shallow part of the plate interface. Sites G03–G06 are located above the SSE source fault that was inferred from the repeating earthquakes (gray box in the top panel of Figure 11a). Tomita (2018) indicated that a time series of the array

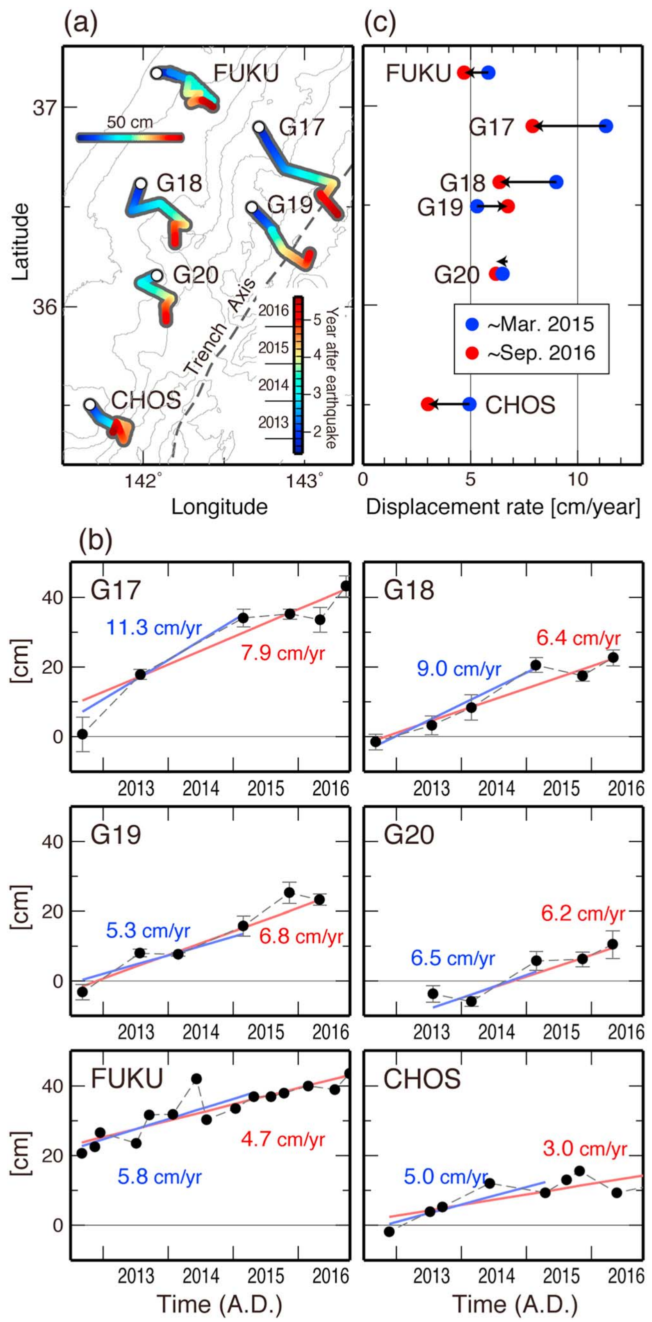

Figure 12. Movement of the six sites in the southern area. (a) Array tracks. Color indicates time. The array position between the campaigns is linearly interpolated. (b) Southeastward array positions (solid circles) and fitted lines to those in the earlier period until March 2015 (blue lines) and the entire period until September 2016 (red lines). (c) Southeastward displacement rates over the earlier period (blue circles) and the entire period (red circles).

positions of sites G03 and G04 possibly contain step discontinuities in early 2015 in agreement with the repeating earthquake study. We attempted to estimate the amount of displacement caused by the SSE based on our reevaluated GPS-A observation results. By using a time series of the array positions of sites G03–G06, the slip amount at each site and a common slip direction were identified along with steady linear movement before and after the SSE for each site (Figure 11a). The timing of the step is CE 2015.1, as inferred from the repeating earthquake study. Despite the low observation frequency, the resulting slip (red arrows) is generally in good agreement with that expected from the repeating earthquakes (black arrows). In addition, we determined that sites G03–G05 likely experienced step motion in early 2015. Following Tomita (2018), we applied three models for the array displacement in the relative plate motion direction (N114°E) of sites G02–G08 (Figure 11b): uniform linear motion (green lines), no movement except a step at CE 2015.1 (red lines), and uniform linear motion and a step (blue lines). The second model, which has only step motion, was found to be the most relevant for sites G03–G05 in the 2015 SSE area by the smallest Akaike information criterion values (highlighted in yellow). Moreover, we confirmed that the step motion was judged relevant for these sites almost only if it occurred at this time, that is, between the third and fourth campaigns (Figure S9 in the supporting information). On the contrary, the first model without a step was found to be most relevant for sites G02, G06, and G07. This does not completely deny the possibility of a step at G06 because the third model, a combination of linear motion and a step, has nearly the same Akaike information criterion value as the first model for the site. Although the third model, with a step, was chosen for site G08, this result has the opposite step direction and therefore was rejected as irrational. Insufficient observation frequency degrades the resolution; however, these results demonstrate the capability of the GPS-A observation for detecting an offshore SSE.

5.4. Southern Area

The relatively large seaward movement of sites G17–G20 in the southern area indicates intensive afterslip that releases accumulated stress in the shallow parts of the plate interface associated with the 2011 earthquake. The average motion direction of these sites was nearly the southeast (N136°E), which deviates by ~20° from the global plate motion direction of the North American plate relative to the Pacific plate (N114°E; Figure 8b). Instead, it is approximately normal to the local strike of the trench axis (section 4.4 and Figure 8a), suggesting that strain partitioning may occur in this area. It has been reported that very large afterslip occurred immediately after the earthquake, which amounts to as much as several tens of centimeters in about 8 months in near-trench areas at 35–37°N (Iinuma et al., 2016). Our results revealed that considerable afterslip in the southern area has been ongoing for ~5 years after the earthquake, although the movement has become significantly more modest than that in the earlier transient period. This declining feature can be recognized even within our observation period. Although we assumed steady linear movement, seaward movement in the southern area appeared to be declining in actuality in a late period of our observations (Figure 12a). In order to confirm this result, we estimated the displacement rates in the southeast direction (N135°E) for the entire period until September 2016 and for an earlier period until Cruise #7 in March 2015 (Figure 12b). Except for that at site G19, higher displacement rates were generally obtained for the early period than for the entire period

(Figures 12b and 12c), suggesting a general decline in afterslip more than 5 years after the earthquake in this area.

The JCG site CHOS located at ~35°N has a significantly smaller displacement rate than that at G17–G20 to the north, indicating that the area of intensive afterslip is limited to the south at ~36°N (Figure 8a) and that the stress may remain unreleased farther south. It worth noting that the site CHOS is located near the possible source region of the 1677 tsunami earthquake that occurred off the Pacific coast of the Boso Peninsula (e.g., Yanagisawa et al., 2016). Similarly, sites G02–G04 in the northern area showed rather small movement and are located in an area in which large earthquakes and tsunamis have been occurring repeatedly, including the 1896 Sanriku tsunami earthquake.

6. Conclusions

We developed an analysis method of GPS-A array positioning that considers a general sloping structure of the sound speed. Its effect on travel time is represented by two independent quantities, the NTD gradient and the directional NTD. The directional NTD affects array positioning in theory. In practice, however, it turned out that incorporating the information of the NTD gradient was necessary to ensure numerical stability. We applied this method and revised our previous results of horizontal movement at our 20 observation sites off the Tohoku region. The revised movement shows greater similarity in direction and rate between neighboring sites, suggesting the enhanced accuracy of the array positions.

The horizontal displacement rate of site G01 on the Pacific plate was rather close to the relative plate motion velocity. This indicates that the effect of viscoelastic relaxation, at 1–2 cm/year, was smaller than that predicted from the existing model of Sun et al. (2014). The movement of the near-trench sites G07–G13 and G15 above the main rupture zone was generally landward and was significantly faster than the relative motion of the Pacific plate, suggesting a considerable contribution of viscoelastic relaxation along with a certain high degree of plate coupling in this region. The viscoelastic relaxation component was estimated to be 5–10 cm/year at these sites when we assume the plate interface was fully locked. The along-trench distribution of the viscoelastic relaxation component was clearly asymmetric, showing a peak near 38°N, at the updip of the mainshock hypocenter, and extending much farther to the north than to the south. This implies the existence of a secondary coseismic slip patch in the north in addition to the primary slip patch at ~38°N.

Afterslip is still occurring to the south of the main rupture zone with relatively large displacement rates, while movement is very small to the north, suggesting different frictional and mechanical properties of the plate interface. The occurrence of episodic slow slip in early 2015 in the northern area, which has been inferred from repeating earthquake data, was also verified by our GPS-A observations. The intensive afterslip in the southern area appears to be limited to the south at ~36°N, near the possible source region of the 1677 tsunami earthquake.

Acknowledgments
This work was supported by activity of the Core Research Cluster of Disaster Science in Tohoku University (a Designated National University). This research was also supported by the project for "Development of GPS/Acoustic Technique," the Ministry of Education, Culture, Sports, Science and Technology (MEXT), Japan, and by the Cross-ministerial Strategic Innovation Promotion Program "Enhancement of societal resiliency against natural disasters," Japan Science and Technology Agency with the Council for Science, Technology and Innovation. This study was also supported by Japan Society for the Promotion of Science (JSPS) KAKENHI Grants JP26000002 and 15K05260 and Earthquake and Volcano Hazards Observation and Research Program by the MEXT, Japan. The array position and displacement rate data are provided in the supporting information. The authors thank T. Sun for allowing use of the calculation results of the viscoelastic relaxation model. R. Hino, Y. Ohta, A. Hasegawa, and K. Yoshida are appreciated for helpful discussion and constructive comments. GMT-SYSTEM (Wessel & Smith, 1995) was used to process the data and to create most of the figures. In addition, we thank Editage (www.editage.jp) for English language editing.

References

Akaike, H. (1980). Likelihood and the Bayes procedure. In J. M. Bernardo, et al. (Eds.), *Bayesian Statistics* (pp. 143–166). Valencia, Spain: University Press.

Altamimi, Z., Collilieux, X., & Métivier, L. (2011). ITRF2008: An improved solution of the international terrestrial reference frame. *Journal of Geodesy*, *85*(8), 457–473. https://doi.org/10.1007/s00190-011-0444-4

Argus, D. F., Gordon, R. G., & DeMets, C. (2011). Geologically current motion of 56 plates relative to the no-net-rotation reference frame. *Geochemistry, Geophysics, Geosystems*, *12*, Q11001. https://doi.org/10.1029/2011GC003751

Bletery, Q., Sladen, A., Delouis, B., Vallée, M., Nocquet, J.-M., Rolland, L., & Jiang, J. (2014). A detailed source model for the Mw9.0 Tohoku-Oki earthquake reconciling geodesy, seismology, and tsunami records. *Journal of Geophysical Research: Solid Earth*, *119*, 7636–7653. https://doi.org/10.1002/2014JB011261

Chadwell, C. D., & Spiess, F. N. (2008). Plate motion at the ridge-transform boundary of the south Cleft segment of the Juan de Fuca Ridge from GPS-Acoustic data. *Journal of Geophysical Research*, *113*, B04415. https://doi.org/10.1029/2007JB004936

Chen, C.-T., & Millero, F. J. (1977). Speed of sound in seawater at high pressures. *The Journal of the Acoustical Society of America*, *62*(5), 1129–1135. https://doi.org/10.1121/1.381646

Colombo, O. L. (1998). Long-distance kinematic GPS. In P. J. G. Teunissen & A. Kleusberg (Eds.), *GPS for geodesy* (pp. 537–567). Berlin, Heidelberg: Springer. https://doi.org/10.1007/978-3-642-72011-6_13

DeMets, C., Gordon, R. G., & Argus, D. F. (2010). Geologically current plate motions. *Geophysical Journal International*, *181*(1), 1–80. https://doi.org/10.1111/j.1365-246X.2009.04491.x

Fujii, Y., Satake, K., Sakai, S., Shinohara, M., & Kanazawa, T. (2011). Tsunami source of the 2011 off the Pacific coast of Tohoku, Japan earthquake. *Earth, Planets and Space*, *63*(7), 815–820. https://doi.org/10.5047/eps.2011.06.010

Fujita, M., Ishikawa, T., Mochizuki, M., Sato, M., Toyama, S., Katayama, M., et al. (2006). GPS/acoustic seafloor geodetic observation: Method of data analysis and its application. *Earth, Planets and Space*, *58*(3), 265–275. https://doi.org/10.1186/BF03351923

Fujiwara, T., Kodaira, S., No, T., Kaiho, Y., Takahashi, N., & Kaneda, Y. (2011). The 2011 Tohoku-Oki earthquake: Displacement reaching the trench axis. *Science*, *334*(6060), 1240. https://doi.org/10.1126/science.1211554

Gagnon, K., Chadwell, C. D., & Norabuena, E. (2005). Measuring the onset of locking in the Peru-Chile trench with GPS and acoustic measurements. *Nature*, *434*(7030), 205–208. https://doi.org/10.1038/nature03412

Hasegawa, A., & Yoshida, K. (2015). Preceding seismic activity and slow slip events in the source area of the 2011 Mw 9.0 Tohoku-Oki earthquake: A review. *Geoscience Letters*, *2*(1). https://doi.org/10.1186/s40562-015-0025-0

Honsho, C., & Kido, M. (2017). Comprehensive analysis of traveltime data collected through GPS-acoustic observation of seafloor crustal movements. *Journal of Geophysical Research: Solid Earth*, *122*, 8583–8599. https://doi.org/10.1002/2017JB014733

Hu, Y., Bürgmann, R., Uchida, N., Banerjee, P., & Freymueller, J. T. (2016). Stress-driven relaxation of heterogeneous upper mantle and time-dependent afterslip following the 2011 Tohoku earthquake. *Journal of Geophysical Research: Solid Earth*, *121*, 385–411. https://doi.org/10.1002/2015JB012508

Ide, S., Baltay, A., & Beroza, G. C. (2011). Shallow dynamic overshoot and energetic deep rupture in the 2011 Mw 9.0 Tohoku-Oki earthquake. *Science*, *332*(6036), 1426–1429. https://doi.org/10.1126/science.1207020

Iinuma, T., Hino, R., Kido, M., Inazu, D., Osada, Y., Ito, Y., et al. (2012). Coseismic slip distribution of the 2011 off the Pacific Coast of Tohoku Earthquake (M9.0) refined by means of seafloor geodetic data. *Journal of Geophysical Research*, *117*, B07409. https://doi.org/10.1029/2012JB009186

Iinuma, T., Hino, R., Uchida, N., Nakamura, W., Kido, M., Osada, Y., & Miura, S. (2016). Seafloor observations indicate spatial separation of coseismic and postseismic slips in the 2011 Tohoku earthquake. *Nature Communications*, *7*(1), 13506. https://doi.org/10.1038/ncomms13506

Ikuta, R., Tadokoro, K., Ando, M., Okuda, T., Sugimoto, S., Takatani, K., et al. (2008). A new GPS-acoustic method for measuring ocean floor crustal deformation: Application to the Nankai Trough. *Journal of Geophysical Research*, *113*, B02401. https://doi.org/10.1029/2006JB004875

Kido, M. (2007). Detecting horizontal gradient of sound speed in ocean. *Earth, Planets and Space*, *59*(8), e33–e36. https://doi.org/10.1186/BF03352027

Kido, M., Fujimoto, H., Miura, S., Osada, Y., Tsuka, K., & Tabei, T. (2006). Seafloor displacement at Kumano-nada caused by the 2004 off Kii Peninsula earthquakes, detected through repeated GPS/acoustic surveys. *Earth, Planets and Space*, *58*(7), 911–915. https://doi.org/10.1186/BF03351996

Kido, M., Osada, Y., Fujimoto, H., Hino, R., & Ito, Y. (2011). Trench-normal variation in observed seafloor displacements associated with the 2011 Tohoku-Oki earthquake. *Geophysical Research Letters*, *38*, L24303. https://doi.org/10.1029/2011GL050057

Kido, M., Osada, Y., Fujimoto, H., & Kaneda, Y. (2007). Monitoring the lateral gradient of sound speed in ocean toward fast GPS/acoustic seafloor positioning for the cabled system. Paper presented at American Geophysical Union Fall Meeting 2007, San Francisco.

Kita, S., Okada, T., Hasegawa, A., Nakajima, J., & Matsuzawa, T. (2010). Anomalous deepening of a seismic belt in the upper-plane of the double seismic zone in the Pacific slab beneath the Hokkaido corner: Possible evidence for thermal shielding caused by subducted forearc crust materials. *Earth and Planetary Science Letters*, *290*(3-4), 415–426. https://doi.org/10.1016/j.epsl.2009.12.038

Locarnini, R. A., Mishonov, A. V., Antonov, J. I., Boyer, T. P., Garcia, H. E., Baranova, O. K., et al. (2013). World Ocean Atlas 2013,Volume 1: Temperature. In S. Levitus & A. Mishonov (Eds.), *NOAA Atlas NESDIS 73* (40 pp.).

Matsui, R., Kido, M., Honsho, C., & Tomita, F. (2018). Spatially non-linear property of sound speed structure in GPS-acoustic measurement. Paper presented at Japan Geoscience Union Meeting 2018, Makuhari, Japan.

Matsumoto, Y., Fujita, M., Ishikawa, T., Mochizuki, M., Yabuki, T., & Asada, A. (2006). Undersea co-seismic crustal movements associated with the 2005 Off Miyagi Prefecture Earthquake detected by GPS/Acoustic seafloor geodetic observation. *Earth, Planets, and Space*, *58*(12), 1573–1576. https://doi.org/10.1186/BF03352663

Nakajima, J., & Hasegawa, A. (2006). Anomalous low-velocity zone and linear alignment of seismicity along it in the subducted Pacific slab beneath Kanto, Japan: Reactivation of subducted fracture zone? *Geophysical Research Letters*, *33*, L16309. https://doi.org/10.1029/2006GL026773

Okada, Y. (1992). Internal deformation due to shear and tensile faults in a half-space. *Bulletin of the Seismological Society of America*, *82*, 1018–1040.

Ozawa, S., Nishimura, T., Munekane, H., Suito, H., Kobayashi, T., Tobita, M., & Imakiire, T. (2012). Preceding, coseismic, and postseismic slips of the 2011 Tohoku earthquake, Japan. *Journal of Geophysical Research*, *117*, B07404. https://doi.org/10.1029/2011JB009120

Romano, F., Trasatti, E., Lorito, S., Piromallo, C., Piatanesi, A., Ito, Y., et al. (2014). Structural control on the Tohoku earthquake rupture process investigated by 3D FEM, tsunami and geodetic data. *Scientific Reports*, *4*(1). https://doi.org/10.1038/srep05631

Sato, M., Ishikawa, T., Ujihara, N., Yoshida, S., Fujita, M., Mochizuki, M., & Asada, A. (2011). Displacement above the hypocenter of the 2011 Tohoku-Oki earthquake. *Science*, *332*(6036), 1395. https://doi.org/10.1126/science.1207401

Spiess, F. N. (1985). Suboceanic geodetic measurements. *IEEE Transactions on Geoscience and Remote Sensing*, *GE-23*(4), 502–510. https://doi.org/10.1109/TGRS.1985.289441

Spiess, F. N., Chadwell, C. D., Hildebrand, J. A., Young, L. E., Purcell, G. H. Jr., & Dragert, H. (1998). Precise GPS/acoustic positioning of seafloor reference points for tectonic studies. *Physics of the Earth and Planetary Interiors*, *108*(2), 101–112. https://doi.org/10.1016/S0031-9201(98)00089-2

Suito, H. (2017). Importance of rheological heterogeneity for interpreting viscoelastic relaxation caused by the 2011 Tohoku–Oki earthquake. *Earth, Planets and Space*, *69*(1). https://doi.org/10.1186/s40623-017-0611-9

Sun, T., Wang, K., Fujiwara, T., Kodaira, S., & He, J. (2017). Large fault sip peaking at trench in the 2011 Tohoku-Oki earthquake. *Nature Communications*, *8*(4044). https://doi.org/10.1038/ncomms14044

Sun, T., Wang, K., Iinuma, T., Hino, R., He, J., Fujimoto, H., et al. (2014). Prevalence of viscoelastic relaxation after the 2011 Tohoku-Oki earthquake. *Nature*, *514*(7520), 84–87. https://doi.org/10.1038/nature13778

Tadokoro, K., Ando, M., Ikuta, R., Okuda, T., Besana, G., Sugimoto, S., & Kuno, M. (2006). Observation of coseismic seafloor crustal deformation due to M7 class offshore earthquakes. *Geophysical Research Letters*, *33*, L23306. https://doi.org/10.1029/2006GL026742

Tomita, F. (2018). *A study on the co- and post-seismic deformation of the 2011 Tohoku-oki earthquake inferred from GPS-acoustic observations, Ph.D. thesis*. Sendai, Japan: Tohoku University.

Tomita, F., Kido, M., Ohta, Y., Iinuma, T., & Hino, R. (2017). Along-trench variation in seafloor displacements after the 2011 Tohoku earthquake. *Science Advances*, *3*(7), e1700113. https://doi.org/10.1126/sciadv.1700113

Tomita, F., Kido, M., Osada, Y., Hino, R., Ohta, Y., & Iinuma, T. (2015). First measurement of the displacement rate of the Pacific Plate near the Japan Trench after the 2011 Tohoku-Oki earthquake using GPS/acoustic technique. *Geophysical Research Letters*, *42*, 8391–8397. https://doi.org/10.1002/2015GL065746

Tsuji, T., Kawamura, K., Kanamatsu, T., Kasaya, T., Fujikura, K., Ito, Y., et al. (2013). Extension of continental crust by anelastic deformation during the 2011 Tohoku-oki earthquake: The role of extensional faulting in the generation of a great tsunami. *Earth and Planetary Science Letters*, *364*, 44–58. https://doi.org/10.1016/j.epsl.2012.12.038

Tsuru, T., Park, J.-O., Miura, S., Kodaira, S., Kido, Y., & Hayashi, T. (2002). Along-arc structural variation of the plate boundary at the Japan Trench margin: Implication of interplate coupling. *Journal of Geophysical Research*, *107*(B12), 2357. https://doi.org/10.1029/2001JB001664

Uchida, N., Honsho, C., Tomita, F., Matsuzawa, T., & Bürgmann, R. (2018). Episodic slow slip after the 2011 Tohoku-oki earthquake: Detection from repeating earthquakes, very low frequency earthquakes, and seafloor geodetic observations. Paper presented at Seismological Society of Japan Fall Meeting 2018, Koriyama, Japan.

Uchida, N., & Matsuzawa, T. (2013). Pre- and postseismic slow slip surrounding the 2011 Tohoku-oki earthquake rupture. *Earth and Planetary Science Letters*, *374*, 81–91. https://doi.org/10.1016/j.epsl.2013.05.021

Wang, K., Sun, T., Brown, L., Hino, R., Tomita, F., Kido, M., et al. (2018). Learning from crustal deformation associated with the M9 2011 Tohoku-oki earthquake. *Geosphere*, *14*(2), 552–571. https://doi.org/10.1130/GES01531.1

Watanabe, S. (2016). Dependency on the sound velocity model for the GPS-acoustic seafloor positioning (in Japanese with English abstract). Reports on Hydrographic Oceanography Research, 53, 82–89.

Watanabe, S., Sato, M., Fujita, M., Ishikawa, T., Yokota, Y., Ujihara, N., & Asada, A. (2014). Evidence of viscoelastic deformation following the 2011 Tohoku-Oki earthquake revealed from seafloor geodetic observation. *Geophysical Research Letters*, *41*, 5789–5796. https://doi.org/10.1002/2014GL061134

Watanabe, S., & Uchida, T. (2016). Stable structures of temperature and salinity validated by the repeated measurements in the few-miles-square regions off Japan coast in the western Pacific [in Japanese with English abstract]. Reports on Hydrographic Oceanography Research, 53, 57–81.

Wessel, P., & Smith, W. H. F. (1995). New version of the generic mapping tools. *Eos, Transactions American Geophysical Union*, *76*(33), 329. https://doi.org/10.1029/95EO00198

Wong, G. S. K., & Zhu, S. (1995). Speed of sound in seawater as a function of salinity, temperature and pressure. *The Journal of the Acoustical Society of America*, *97*(3), 1732–1736. https://doi.org/10.1121/1.413048

Yabuki, T., & Matsu'ura, M. (1992). Geodetic data inversion using a Bayesian information criterion for spatial distribution of fault slip. *Geophysical Journal International*, *109*(2), 363–375. https://doi.org/10.1111/j.1365-246X.1992.tb00102.x

Yamagiwa, S., Miyazaki, S., Hirahara, K., & Fukahata, Y. (2015). Afterslip and viscoelastic relaxation following the 2011 Tohoku-oki earthquake (Mw9.0) inferred from inland GPS and seafloor GPS/Acoustic data. *Geophysical Research Letters*, *42*, 66–73. https://doi.org/10.1002/2014GL061735

Yanagisawa, H., Goto, K., Sugawara, D., Kanamaru, K., Iwamoto, N., & Takamori, Y. (2016). Tsunami earthquake can occur elsewhere along the Japan Trench—Historical and geological evidence for the 1677 earthquake and tsunami. *Journal of Geophysical Research: Solid Earth*, *121*, 3504–3516. https://doi.org/10.1002/2015JB012617

Yasuda, K., Tadokoro, K., Ikuta, R., Watanabe, T., Nagai, S., Okuda, T., et al. (2014). Interplate locking condition derived from seafloor geodetic data at the northernmost part of the Suruga Trough, Japan. *Geophysical Research Letters*, *41*, 5806–5812. https://doi.org/10.1002/2014GL060945

Yasuda, K., Tadokoro, K., Taniguchi, S., Kimura, H., & Matsuhiro, K. (2017). Interplate locking condition derived from seafloor geodetic observation in the shallowest subduction segment at the Central Nankai Trough, Japan. *Geophysical Research Letters*, *44*, 3572–3579. https://doi.org/10.1002/2017GL072918

Yokota, Y., Ishikawa, T., & Watanabe, S. (2018a). Gradient field of undersea sound speed structure extracted from the GNSS-A oceanography. *Marine Geophysical Research*. https://doi.org/10.1007/s11001-018-9362-7

Yokota, Y., Ishikawa, T., & Watanabe, S. (2018b). Seafloor crustal deformation data along the subduction zones around Japan obtained by GNSS-A observations. *Scientific Data*, *5*, 180182. https://doi.org/10.1038/sdata.2018.182

Yokota, Y., Ishikawa, T., Watanabe, S., Tashiro, T., & Asada, A. (2016). Seafloor geodetic constraints on interplate coupling of the Nankai Trough megathrust zone. *Nature*, *534*(7607), 374–377. https://doi.org/10.1038/nature17632

Zweng, M. M., Reagan, J. R., Antonov, J. I., Locarnini, R. A., Mishonov, A. V., Boyer, T. P., et al. (2013). World Ocean Atlas 2013, Volume 2: Salinity. In S. Levitus & A. Mishonov (Eds.), *NOAA Atlas NESDIS 74* (39 pp.).